Dynamical and Microphysical Retrieval from Doppler Radar Observations Using a Cloud Model and Its Adjoint. Part II: Retrieval Experiments of an Observed Florida Convective Storm

JUANZHEN SUN AND N. ANDREW CROOK

National Center for Atmospheric Research, Boulder, Colorado*

(Manuscript received 28 February 1997, in final form 22 July 1997)

ABSTRACT

The variational Doppler radar analysis system developed in part I of this study is tested on a Florida airmass storm observed during the Convection and Precipitation/ Electrification Experiment. The 3D wind, temperature, and microphysical structure of this storm are obtained by minimizing the difference between the radar-observed radial velocities and rainwater mixing ratios (derived from reflectivity) and their model predictions. Retrieval experiments are carried out to assimilate information from one or two radars. The retrieved fields are compared with measurements of two aircraft penetrating the storm at different heights.

The retrieved wind, thermodynamical, and microphysical fields indicate that the minimization converges to a solution consistent with the input velocity and rainwater fields. The primary difference between using single-Doppler and dual-Doppler information is the reduction of the peak strength of the storm on the order of 10% when information from only one radar is provided. The comparison with aircraft data shows good agreement for the vertical velocity, buoyancy, and the water vapor mixing ratio in terms of the general structure and strength of the fields, but less agreement for the cloud water and rainwater field. The sensitivities of the retrieval system to the neglect of the time difference at each grid point in a radar volume and to the inclusion of the background information at the initial time of the assimilation period are examined. Both show rather sensitive response. The experiments also show that the microphysical retrieval is quite sensitive to the relation used to derive the rainwater mixing ratio from reflectivity observations.

1. Introduction

In part I of this study, the variational Doppler radar analysis system (VDRAS) for retrieval of three-dimensional wind, thermal, and hydrometeor fields was described and tested using simulated data of a warm rain convective storm (Sun and Crook 1997, hereafter referred to as SC97). This analysis system applies the 4D variational data assimilation technique to a cloud-scale model. Radial velocity and reflectivity observations from one or more Doppler radars can be assimilated into the numerical model by minimizing the difference between the observations and the model predictions. A set of optimal initial conditions consisting of wind, thermal, and microphysical fields is determined as the model is optimally fitted to the observations. This new Doppler radar analysis technique differs from traditional analysis techniques (Gal-Chen 1978; Hane and Scott 1978; Hanes et al. 1981; Roux 1985; Rutledge and Hobbs 1983, 1984; Ziegler 1985; Hauser and Amayenc 1986) in one fundamental respect, which is that the model variables are determined simultaneously in a dynamically consistent way, whereas the traditional techniques find these fields sequentially. The application of this analysis system to different stages of the evolution of a simulated convective storm demonstrated that the detailed structure of wind, thermodynamics, and microphysics could be obtained with reasonable accuracy. The experiments in part I also demonstrated that the on–off switches existing in the moist processes did not cause any problem in the minimization procedure. Techniques were developed in SC97 to avoid the problem of high nonlinearity associated with some of the moist processes.

Although the encouraging results obtained in the simulated data study suggested that information of the unobserved meteorological fields could be derived from a time history of the radial velocity and reflectivity observations with the aid of a cloud-scale numerical model, the application of VDRAS to observed convective storms can still present a great challenge. There are three major concerns when applying the technique to real data. First, unlike simulated data, which cover the entire integration domain, radar observations are confined to

* The National Center for Atmospheric Research is sponsored by the National Science Foundation.

Corresponding author address: Dr. Juanzhen Sun, National Center for Atmospheric Research, Boulder, CO 80307.
E-mail: sunj@ncar.ucar.edu

© 1998 American Meteorological Society

the region where reflectors exist and there are generally large areas without data. Second, the model does not always represent the atmosphere accurately, mainly due to the simplified microphysical parameterization schemes in the cloud model. Third, the reflectivity of hydrometeors is related to the model rainwater through a presumed Z–q_r relation and this relation can contain significant error.

In this paper, we use radar observations of a Florida airmass storm to examine the applicability of the retrieval technique in VDRAS to real data. The data were collected during the Convective and Precipitation/Electrification Experiment (CaPE). Measurements from three radars (CP-2, CP-3, and CP-4) were available. The retrieval experiments are performed using observations from either single-Doppler (CP-3 or CP-4) or dual-Doppler radars (CP-3 and CP-4). The retrieved fields are compared with measurements from two aircraft penetrating the storm.

The data source and the processing procedure will be described in the next section. Since the cloud model and the variational analysis technique have been described in part I of this study, in this paper only the main points and the recent refinement will be presented in section 3. In section 4, results of the retrieval will be discussed. Comparison of these results with aircraft measurements will be given in section 5. Finally, the summary and discussions will be offered in section 6.

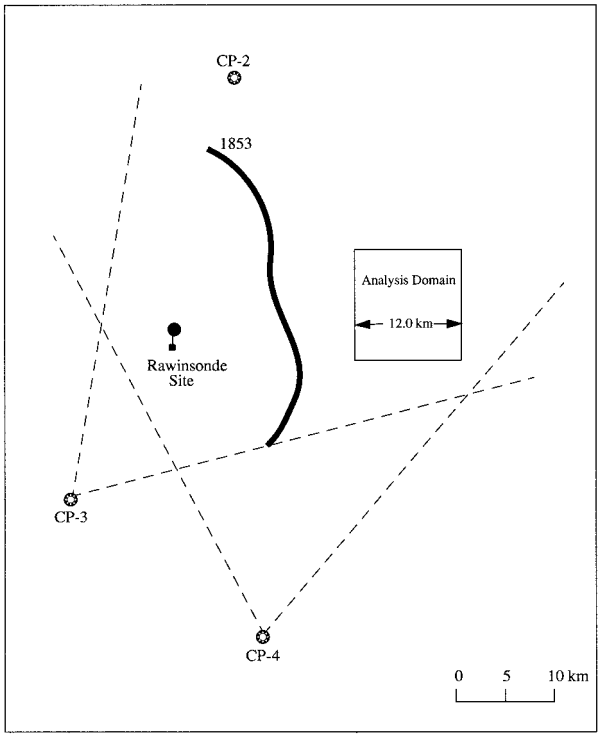

FIG. 1. Positions of CP-2, CP-3, and CP-4; the approximate sector scan regions of CP-3 and CP-4; and the location of the analysis domain. The location of the upper air sounding site at Tico airport and the position of the sea breeze front (thick black line) at 1853 UTC are also shown.

2. Data and processing procedure

CaPE was conducted in east-central Florida during the summer of 1991. Data systems of primary importance to this study are the C-band Doppler radars (CP-3 and CP-4), which provide radial velocity and reflectivity observations for the retrieval experiments. On 26 July, when the storm of interest occurred, both radars performed sector scans within the northeastern dual-Doppler lobe (Fig. 1). In addition to these two radars, a third radar, CP-2, which mainly performed RHI (range-height indicator) scans provided differential reflectivity (Z_{DR}) and dual-frequency measurements. Atmospheric sounding data were provided by the mobile and stationary National Center for Atmospheric Research (NCAR) CLASS sounding systems. Two aircraft, the NCAR King Air (N312D) and the University of Wyoming King Air (N2UW), flew through the storms at different altitudes providing measurements along the flight tracks.

The storm of interest occurred on the afternoon of 26 July 1991 and was initiated along a sea breeze boundary. The evolution, kinematic structure, and convective initiation of this sea breeze front was studied in detail by Laird et al. (1995). The position of the sea breeze at 1853 UTC is depicted in Fig. 1. The sounding taken at Tico airport west of the sea breeze front at 1905 UTC is shown in Fig. 2 (smoothed from the original data). It is seen that the boundary layer (below 870 mb) wind is from the south-southwest at about 4 m s^{-1}. The synoptic flow immediately above the boundary layer is from the southwest. The sounding also shows a lifting condensation level of 1.6 km and a layer of high stability centered at 6 km that restricts the convective available potential energy to about 300 J kg^{-1}. A series of convective cells developed throughout the early afternoon (1700–1915 UTC) along the convergence zone of the sea breeze front while the sea breeze propagated inland (westward). The particular convective cell studied in this paper developed around 1900 UTC in a region of enhanced convergence along the sea breeze front. This convective cell then moved northeastward with the ambient flow above the sea breeze at a speed of around 5.5 m s^{-1}. The evolution of this storm is illustrated by the reflectivity contours at the 4.2-km level in Fig. 3. The maximum reflectivity exceeds 50 dBZ at the peak of the storm development. As seen from Fig. 3, this storm is characterized as a two-cell system (C1 and C2). During the period shown, the southern cell (C1) decays as cell C2 develops rapidly between 1905 and 1919 UTC. The lifetime of this system is around 30 min. Due to the layer of high stability around 6 km, the system did not develop significantly above this level. Both the temperature profile and the differential reflectivity observations from CP2 indicate that warm rain processes dominate in the convection system. We purposely chose

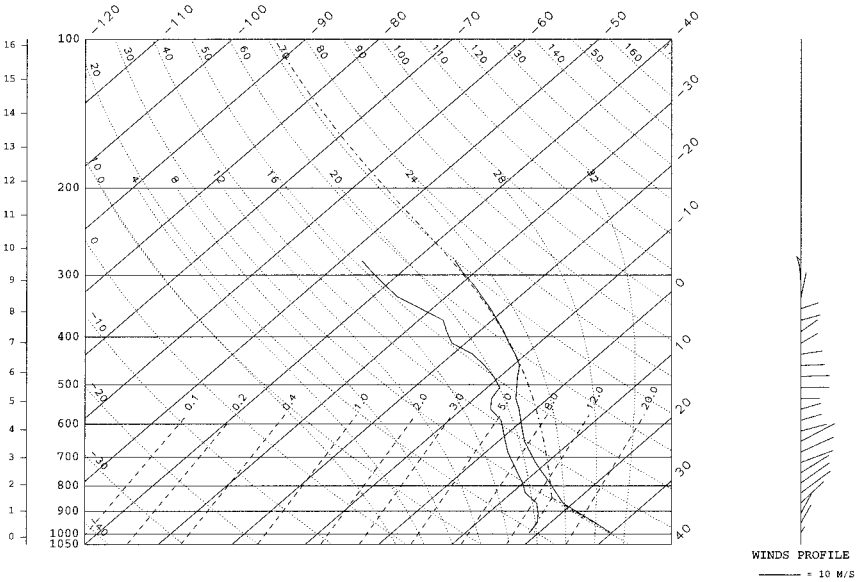

FIG. 2. Sounding taken from at Tico airport at 1905 UTC. Temperature and dewpoint are shown on a skew-*T* plot. Altitude (km) and pressure (mb) scales appear on the left side. The wind profile is shown on the right side.

this storm because it can better fit our warm rain cloud model. Fankhauser and Breed (1995) documented the kinematical structure of this storm through Doppler radar synthesis and microphysical measurements of the two King Airs. Barnes et al. (1992) and Barnes and Browning (1993) examined the mixing process of this storm system using aircraft analyses.

The radars provide radial velocity and reflectivity data sampled in spherical coordinates. Since the numerical model was written in Cartesian coordinates, it is necessary to interpolate the data from a spherical grid to a Cartesian grid. The algorithm used to perform the interpolation was SPRINT (sorted position radar interpolation) (Mohr and Vaughan 1979; Miller et al. 1986). This interpolation algorithm applies a piecewise-continuous, bilinear scheme with local unfolding of radial velocities. The data were interpolated to a grid with 200-m resolution in all three directions. The size and position of the analysis domain is illustrated in Fig. 1. Other than the radial velocity and reflectivity data, the output fields from SPRINT also include the signal to noise ratio and a quality field, a measure of the quality of the interpolated value according to the sample standard deviation. Since the interpolation was applied to the radar data without prior editing, these two fields will be used later in the Cartesian grid to reject unreliable velocity data.

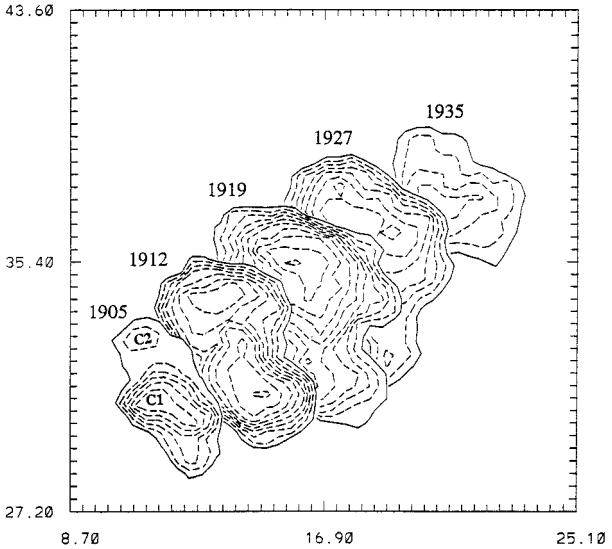

FIG. 3. Radar reflectivity contours at 4.2 km (increasing from 0 dB in 5-dB steps) illustrating the evolution of the storm in the 30-min lifetime of cell C2.

After the spatial interpolation, the data were processed using CEDRIC (custom editing and display of reduced information in Cartesian space) (Mohr et al. 1986). The radial velocity data were first edited requiring a threshold value of the signal to noise ratio. Then the quality field was applied to further reject very noisy data. In this editing procedure, we attempted to eliminate data dominated by noise while retaining as much information as possible. The remaining data of poorer quality were given a smaller weight through the weighting coefficient in the cost function (defined in the next section). After the above editing procedure was applied, the missing data were filled using a two-dimensional, linear, local least squares method. This data-filling procedure was only applied to points surrounded by data in at least three quadrants. Finally numerical

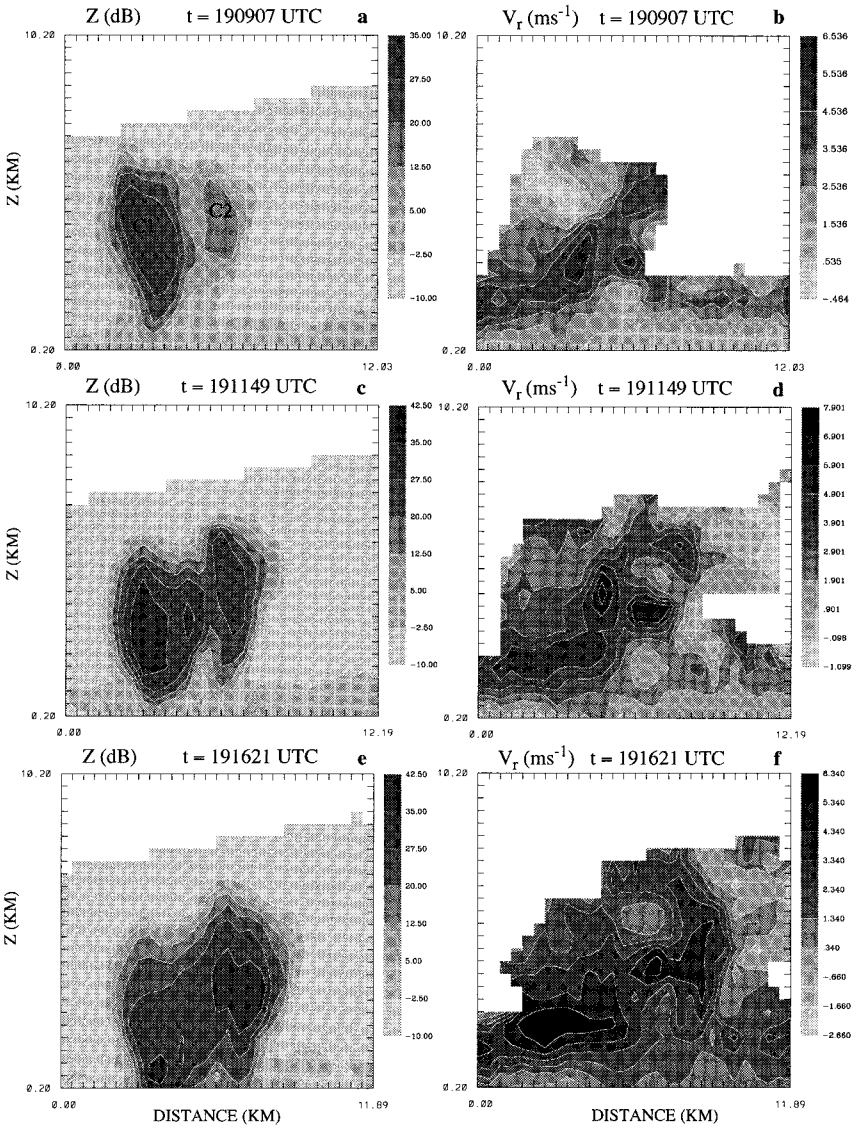

FIG. 4. Vertical cross sections of the observed reflectivity (left) and radial velocity (right) from CP-4 at 1909:07 UTC [(a) and (b)], 1911:49 UTC [(c) and (d)], and 1916:21 UTC [(e) and (f)]. The cross sections are through the centers of the two cells as viewed from the direction of the storm propagation.

smoothing by one pass of a Leise filter (Leise 1981) was performed to reduce random noise in the radial velocity data. It should be noted that the data filling and numerical smoothing are not absolutely necessary. However, we have found that these procedures can generally improve the convergence of the minimization algorithm procedure.

Three volume scans from CP-3 and CP-4 were used in the retrieval experiments. In Fig. 4, the reflectivity and radial velocity data from CP-4 for the three volumes are displayed by vertical cross sections through the center of the storm. The times on the top of each panel, t = 1909:07, t = 1911:49, and t = 1916:21 UTC, are the midpoint times for the three data volumes. Each volume took around 2.5 min to complete. The beginning and end times of the three volume scans from CP-4 are given in the following:

V1: 1907:53–1910:24 UTC;

V2: 1910:34–1913:04 UTC;

V3: 1915:06–1917:37 UTC.

It should be noted that CP-4 lagged CP-3 by approximately 10 s. This difference is ignored and the midpoint time of each volume scan from CP-4 was used to represent the observational time of each volume throughout this paper. The reflectivity fields clearly show the two-cell structure of the storm with cell C1 decaying and

cell C2 growing. Although the radial velocity changes significantly from one volume to the rest, the main features can be well identified. Figure 4 also shows that there are large areas void of data in the radial velocity field. In the next section, we will describe a method to fill in these regions. Since very noisy data in the radial velocity field were rejected, the data-void regions in velocity are larger than those for reflectivity.

3. The VDRAS technique and recent refinement

The technique of VDRAS was described in detail in SC97. The technique was refined recently to be more suitable for assimilating observed Doppler radar data. In this section, we will give a brief review of the technique and discuss the recent refinement of the system.

VDRAS was designed to assimilate a time series of observations (radial velocity and reflectivity) from single or multiple Doppler radars. A cloud model is used to represent the evolution of the motion between radar volumes. At present, the model's microphysical parameterization contains only warm rain processes. There are six prognostic variables in this model: u, v, w (velocities), θ_l (liquid water potential temperature), q_r (rainwater mixing ratio), and q_t (total water mixing ratio). The perturbation pressure (p) and temperature (T), water vapor mixing ratio, and cloud water mixing ratio are diagnostic variables. The objective is to find an initial state of the model that can, upon model integration, produce output parameters matching the radar observations at all times as closely as possible. The misfit between the model and the observations is measured by the cost function defined as

$$J = \sum_{\sigma,\tau,i} [\eta_v(V_{ri} - V_{ri}^{\text{ob}})^2 + \eta_q(q_r - q_{r_i}^{\text{ob}})^2] + J_b + J_p, \tag{3.1}$$

where the summation is over the spatial domain σ, the assimilation period τ, and the radar number i. Here, J_b and J_p represent the background term and penalty term, respectively. They will be explained later in this section. The quantity q_r is the model predicted rainwater mixing ratio in units of g kg^{-1}. The radial velocity V_{ri} in Eq. (3.1) is calculated using the Cartesian velocity components (u, v, w) from the model integration through the following relation:

$$V_{ri} = u\frac{x - x_i}{r_i} + v\frac{y - y_i}{r_i} + (w - V_{\text{Tm}})\frac{z - z_i}{r_i}, \tag{3.2}$$

where V_{Tm} is the mass-weighted terminal velocity of the precipitation, which is given by

$$V_{\text{Tm}} = 5.40aq_r^{0.125}. \tag{3.3}$$

The variable r_i is the distance between a grid point (x, y, z) and the ith radar location (x_i, y_i, z_i). The quantity a is a correction factor defined by $a = (p_0/\overline{p})^{0.4}$, where $\overline{p}$ is the base state pressure and p_0 is the pressure at the ground. The quantities V_{ri}^{ob} and q_{ri}^{ob} in Eq. (3.1) represent observations of radial velocity and rainwater mixing ratio of the ith radar. Note that q_{ri}^{ob} is not a direct observable quantity but is derived from the reflectivity observations using the following Z–q_r relation:

$$Z = 2.04 \times 10^4(\rho q_r)^{1.75}. \tag{3.4}$$

This relation was derived analytically by assuming the Marshal–Palmer distribution of raindrop size with $n_0 = 8 \times 10^6$ mm^{-4}. Since the experiments in SC97 showed that assimilating q_r produced slightly better results than directly assimilating reflectivity data, we use q_r derived from Z as the input data throughout this study. Care must be exercised when converting the reflectivity observations in the boundary layer to the rainwater mixing ratio using Eq. (3.4) because the reflectivity signal in the boundary layer can come either from hydrometeors or from clear-air reflectors (for instance, insects). By carefully examining the data, we found that most clear-air echoes gave reflectivity values less than 5 dBZ (see Fig. 4). Therefore, in the boundary layer, only reflectivity observations greater than 5 dBZ were converted to rainwater mixing ratio using Eq. (3.4). The rainwater mixing ratio was set to zero if the reflectivity was less than 5 dBZ (corresponding to the mixing ratio of 0.007 g kg^{-1}).

In the cost function (3.1), we have assumed that the observational errors are uncorrelated in space and time. Under this assumption, the error covariance matrix in a cost function can be reduced to a diagonal matrix. In Eq. (3.1), we use η_v and η_q to represent the elements of the diagonal matrices. Here, η_v and η_q can also be regarded to as weighting coefficient. They should reflect the relative precision of the data (measurement uncertainty and representativeness error). These two quantities can be further expressed as

$$\eta_v = \sigma_v^{-2}S_v \quad \text{and} \quad \eta_q = \sigma_q^{-2}S_q, \tag{3.5}$$

where σ_v^2 and σ_q^2 are the error variances of the radial velocity and rainwater mixing ratio, respectively. Here, S_v and S_q are dimensional constants. These constants were assumed to be proportional to the reciprocal of the variance of their corresponding observational field. The variance of the observed radial velocity field is about two orders greater than that of the observed rainwater mixing ratio field. Therefore, S_v and S_q were set to 1 and 100, respectively.

The most common errors in radar data are the calibration error in reflectivity and the random noise in radial velocity. A comparison of the reflectivity from CP3 and CP4 revealed that the difference was less than 3 dB. Although the calibration error can have a significant impact on the retrieval (see SC97), in practice it is difficult to determine this error, because the absolute calibration is unknown. In this study, therefore, we are forced to neglect the reflectivity calibration error by setting σ_q^2 to 1. As for the radial velocity error, the sampling local radial velocity variance was employed to approximate the error variance σ_v^2, since noisy data

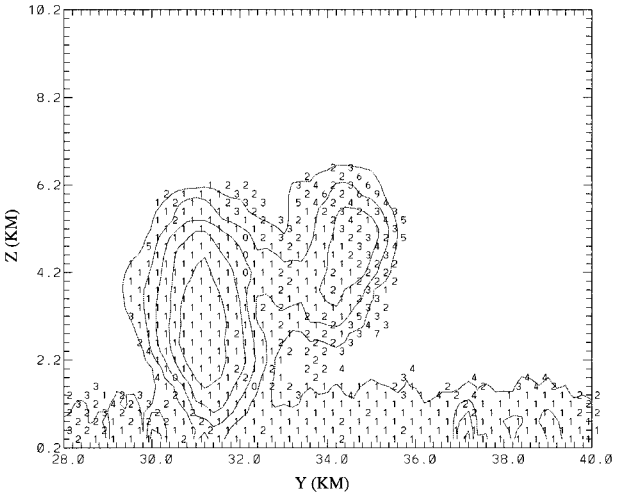

FIG. 5. Numerical values of the standard deviation of the radial velocity in a *y–z* cross section at 1911:49 UTC. The reflectivity contours (increasing from 0 dB in 10-dB steps) are superimposed.

are usually associated with high values of radial velocity variance. The sampling local radial velocity variance was calculated using the radial velocity measurements affecting a grid point in the interpolation from radar geometry to a Cartesian grid. The radial velocity variance is only an approximation of the error variance σ_v^2 because it reflects variability not only from data error, but also from large spatial gradients in the radial velocity field. In Fig. 5, the numerical values of the calculated standard deviation of the radial velocity observations (after the processing procedure described in the last section) are shown along with the reflectivity in a *y–z* cross section through the storm at t = 1911:49 UTC. In general, the standard deviation decreases as the reflectivity increases. The value of zero that appears at a few grid points in this figure represents an actual value between 0 and 0.5. To avoid an excessively large weighting coefficient, any value smaller than 0.5 was set to 0.5.

The quantity J_p in the cost function (3.1) represents the spatial and temporal smoothness penalty functions. The formulation and effect of these functions were discussed by Sun and Crook (1994). The variable J_b in Eq. (3.1) denotes the background term. As discussed in SC97, the general form of the background term can be written as

$$J_b = (\mathbf{x} - \mathbf{x}_b)^{\mathrm{T}}\mathbf{B}^{-1}(\mathbf{x} - \mathbf{x}_b), \tag{3.6}$$

where $\mathbf{x}$ represents model variables in vector form, $\mathbf{x}_b$ stands for background information, the superscript T is the transpose symbol, and $\mathbf{B}$ is the covariance matrix of the background error. In this study, we consider two types of background: one is the mean state represented by the upper-air soundings; the other is the model prediction from the previous assimilation period. Assuming that the matrix $\mathbf{B}$ is diagonal, the mean state background term is defined as

$$J_{bs} = \sum_{\sigma,\tau,m} \eta_m (x_m - \overline{x_m})^2, \tag{3.7}$$

where x_m represents any model variable and $\overline{x_m}$ is the mean profile of this variable from the sounding. The quantity η_m is the weighting constant, or the diagonal element of the covariance matrix $\mathbf{B}$. It is set to zero in the radar data–rich region and has a specified value in the region of vanishing radar echoes. Similarly, if we assume the error covariance matrix is diagonal, the model background term is given by

$$J_{bm} = \sum_{\sigma,\tau,m} \eta_{0m} (x_m - x_m^0)^2, \tag{3.8}$$

where x_m^0 is the model prediction of x_m at the end of the previous assimilation window and η_{0m} is its weighting constant.

The effect of the background term J_{bs} has been examined in SC97. We included this term in all the retrieval experiments presented in the next section by setting η_m to 1 for all variables, the same as the dimensional constant of radial velocity, S_v. The effect of the background term J_{bm} was tested in one of the retrieval experiments described in the next section. The choice of η_{0m} will be discussed there.

Radar data from a volume scan are often taken as a snapshot at a given time. In fact, these data are collected through sequential scanning. The field recording the actual observational time of each data point can be interpolated onto the Cartesian grid along with the observational fields. Our model code was previously written to assimilate any volume of radar data at a fixed time step. In this study, we have modified the code so that it is able to assimilate the radar data at each grid point at the actual observational time. Since the model integration has a time step of 10 s, the actual time field of the observation had to be projected to one that is grouped every 10 s. Instead of assuming the whole data volume at a single time step, only a slice of data at each vertical level is assimilated at each time step. The time field of CP-4 is shown by a south–north cross section in Fig. 6. The values shown in the figure represent the times (in seconds) relative to the beginning time of the volume scan. In the next section, we will conduct experiments to compare these two data injection methods, that is, input the data volume at a single time step or read each grid point observation at the time step it is closest to.

4. Retrieving observed storm structure

The model domain used to perform the retrieval experiments is 11.2 × 11.2 × 10.6 km^3, a subdomain of the analyses domain shown in Fig. 1. The grid spacing is 400 m in the horizontal and 500 m in the vertical. The time step of the model integration is 10 s. The assimilation experiments use two volumes of data with the assimilation window determined by the time interval between these two data volumes. In Fig. 7, the two

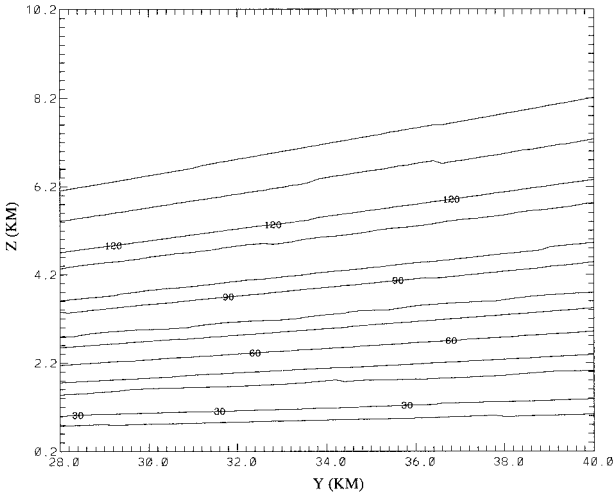

FIG. 6. The time field of V2 plotted in the same cross section as in Fig. 5. The labels on the contours are the time in seconds relative to the beginning time of the volume scan.

assimilation periods along with the midpoint times and the time spans of the radar volume scans are illustrated. Also shown in Fig. 7 are the two aircraft penetration times and heights. Since the aircraft penetrated the center of the storm during the assimilation period II, we will focus our experiments on this period so that we can compare the results with the aircraft observations. Therefore, most experiments described below use data volumes V2 and V3 from both radars unless otherwise noted. The first-guess fields for these retrieval experiments were determined using the procedure described in SC97.

Four experiments have been conducted to retrieve the storm structure using the processed radial velocity and reflectivity data. The first experiment can be viewed as a control experiment (experiment CTR). This experiment includes two runs. Run 1 assimilates data volumes V1 and V2 in the assimilation period I, and run 2 assimilates data volumes V2 and V3 in the assimilation period II. Data in these volume scans are assimilated at the time step they actually correspond to, as opposed to assimilation of the whole radar volume at a fixed time step. Note that the assimilation periods start from the beginning time of the first volume and end at the final time of the second volume. Therefore, the assimilation period I has a total time of 5 min and 11 s, while period II has a total time of 7 min and 3 s. Both CP-3 and CP-4 data are used in this experiment. The sounding background term J_{bs} is included in the cost function but the background term J_{bm} based on a previous retrieval is not. The other three experiments are intended to test the sensitivity of the retrieval system to a few variations. These experiments involve i) assimilating data volumes V2 and V3 from only one radar, CP-4 (experiment SGL); ii) same as the control experiment, but the data volume V2 and V3 are injected at two fixed time steps (the start and the end of the assimilation period), respectively (experiment NTF); and iii) adding the background term J_{bm} in the second assimilation period by using the retrieval from the first assimilation period (experiment BKG). All the retrieval experiments indicated that the minimization converged to a solution consistent with the input velocity and rain water fields. Figure 8 shows the reduction of the normalized cost function with respect to the number of iterations from run 1 of experiment CTR. The cost function decreases rapidly during the first 40 iterations and levels off thereafter. All the experiments presented here employed 100 iterations.

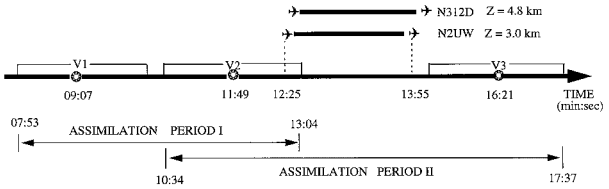

FIG. 7. Diagram illustrating the midtimes and the coverage times of the radar volumes V1, V2, and V3, the period of the aircraft data used for the comparison, and the two assimilation periods. Times shown are minutes and seconds (MMSS) after 1900 UTC.

a. Control experiment

The retrieval results from experiment CTR are illustrated by Figs. 9–11. In Fig. 9, the retrieved fields at 1911:49 UTC (midtime of V2) and at 1916:21 UTC (midtime of V3) are shown by horizontal cross sections at the 3.0-km level. A 5.5 m s^{-1} storm motion vector in a direction of 74° from north has been removed from the original retrieved wind vector. Superimposed on the storm-relative wind vectors are the vertical velocity contours (Figs. 9a,b) and the rainwater mixing ratio (Figs.

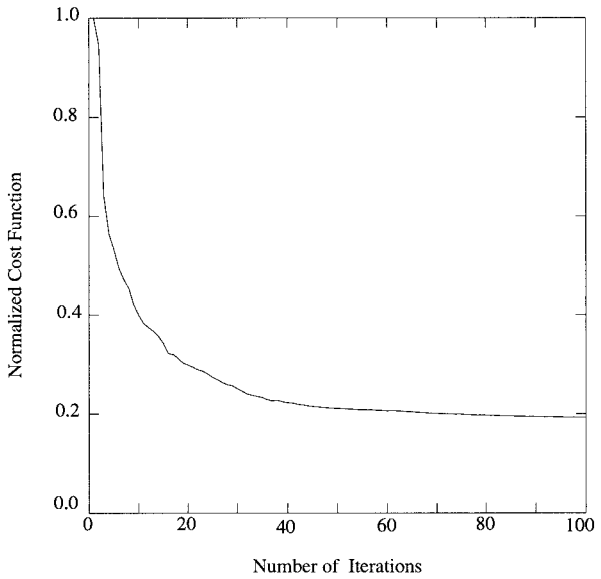

FIG. 8. Normalized cost function as a function of the number of iterations for run 1 of experiment CTR.

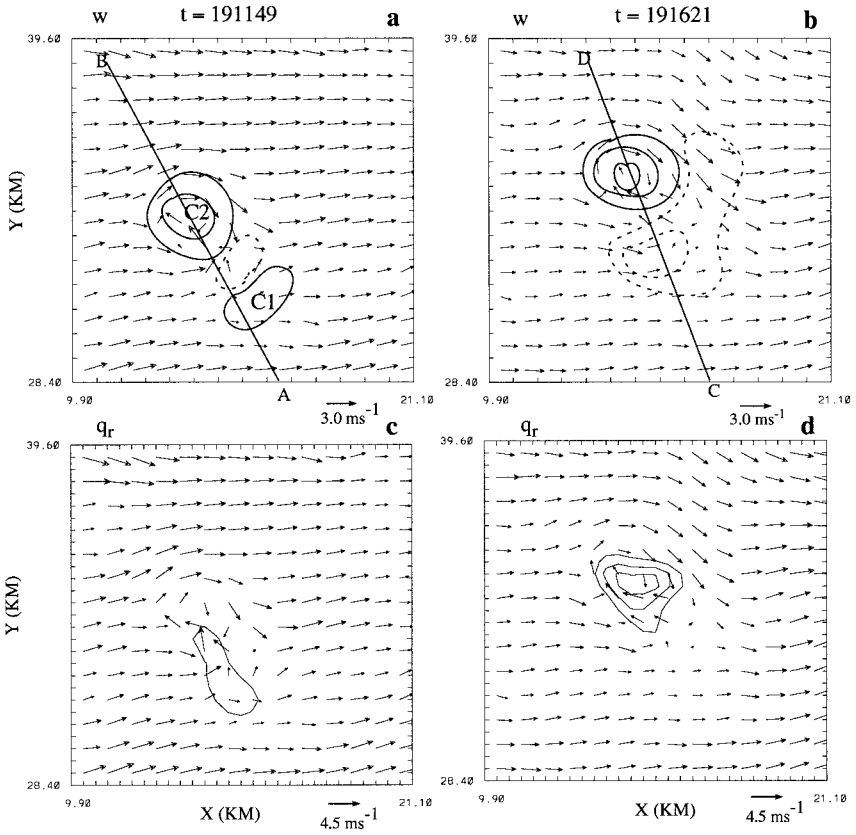

FIG. 9. Horizontal cross sections of the retrieved vertical velocity (upper) and rainwater mixing ratio (lower) and the horizontal velocity vector at $z = 3.0$ km at 1911:49 UTC [(a) and (c)] and 1916:21 UTC [(b) and (d)] from experiment CTR. The ± 1 m s^{-1}, ± 3 m s^{-1}, and $+5$ m s^{-1} contours are shown for the vertical velocity. The contours for rainwater mixing ratio increase from 0.5 g kg^{-1} with a step of 0.5 g kg^{-1}. Straight lines denote the locations of vertical cross sections AB and CD.

9c,d). The most apparent feature from the wind field is the vorticity couplet embedded in the prevailing westerly flow. Although not clearly shown in the horizontal velocity vector field, the two-cell structure is indicated in the vertical velocity field at 1911:49 UTC. There are two updraft centers marked by C1 and C2 in Fig. 9a. At 1916:21, the updraft of the cell C1 is replaced by a downdraft as it dissipates. Meantime, the new cell (cell C2) in the northwest develops rapidly and rainwater of more than 1.5 g kg^{-1} is formed in the updraft.

The retrieved fields at 1911:49 UTC and at 1916:21 UTC from experiment CTR are further illustrated in Figs. 10 and 11, respectively, by vertical cross sections through the updraft core, AB and CD, whose locations are noted in Fig. 9. The cloud top is restricted to between 6 and 7 km by the upper-level stable layer (see Fig. 2). The cloud base (Fig. 10e) agrees quite well with the lifting condensation level of 1.6 km determined from the sounding. At 1911:49 UTC, the velocity fields show two updraft centers. The weaker updraft is associated with a small amount of cloud water but a large amount of rainwater. In contrast, the stronger updraft corresponds to high cloud water content but little rainwater content, suggesting that this cell is in the early developing stage. Both updraft cores are characterized by positive buoyancies. The negative temperature perturbation at cloud top is caused by adiabatic cooling while that at cloud base may be associated with both adiabatic cooling and evaporative cooling. The perturbation water vapor mixing ratio shows a maximum of 2.7 g kg^{-1}, approximately collocated with the center of the rainwater mixing ratio. About 5 min later, at 1916:21 UTC, the structure of the storm has changed considerably. A downdraft of about 3 m s^{-1} has developed near the ground. Associated with this downdraft is evaporative cooling near the ground and precipitation reaching the ground. The updraft associated with C2 weakens in response to rainwater drag despite the fact that the thermal buoyancy is increasing. The rainwater mixing ratio in C2 increases rapidly during the assimilation period II, reaching a maximum of 1.66 g kg^{-1} near the end of this period.

b. Single Doppler retrieval

Figure 12 shows the retrieved fields from experiment SGL in the same vertical cross section as in Fig. 11.

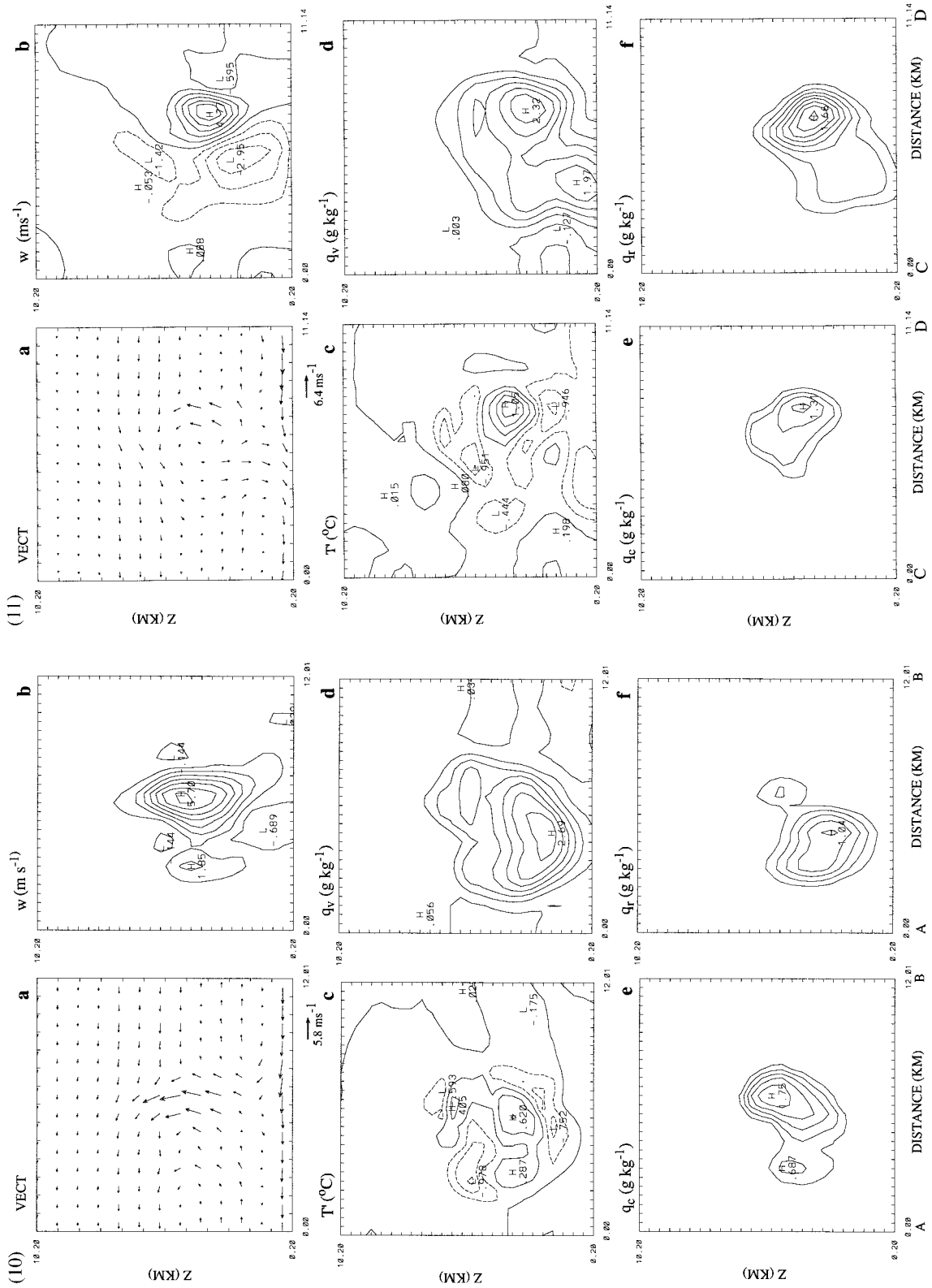

FIG. 10. Vertical cross sections of retrieved fields along AB, as indicated in Fig. 9, at 1911:49 UTC from run 1 of experiment CTR. (a) Velocity vector; (b) vertical velocity in m s^{-1}; (c) perturbation temperature in °C; (d) water vapor mixing ratio in g kg^{-1}; (e) cloud water mixing ratio in g kg^{-1}; and (f) rainwater mixing ratio in g kg^{-1}.

FIG. 11. Same as Fig. 10 but at 1916:21 UTC.

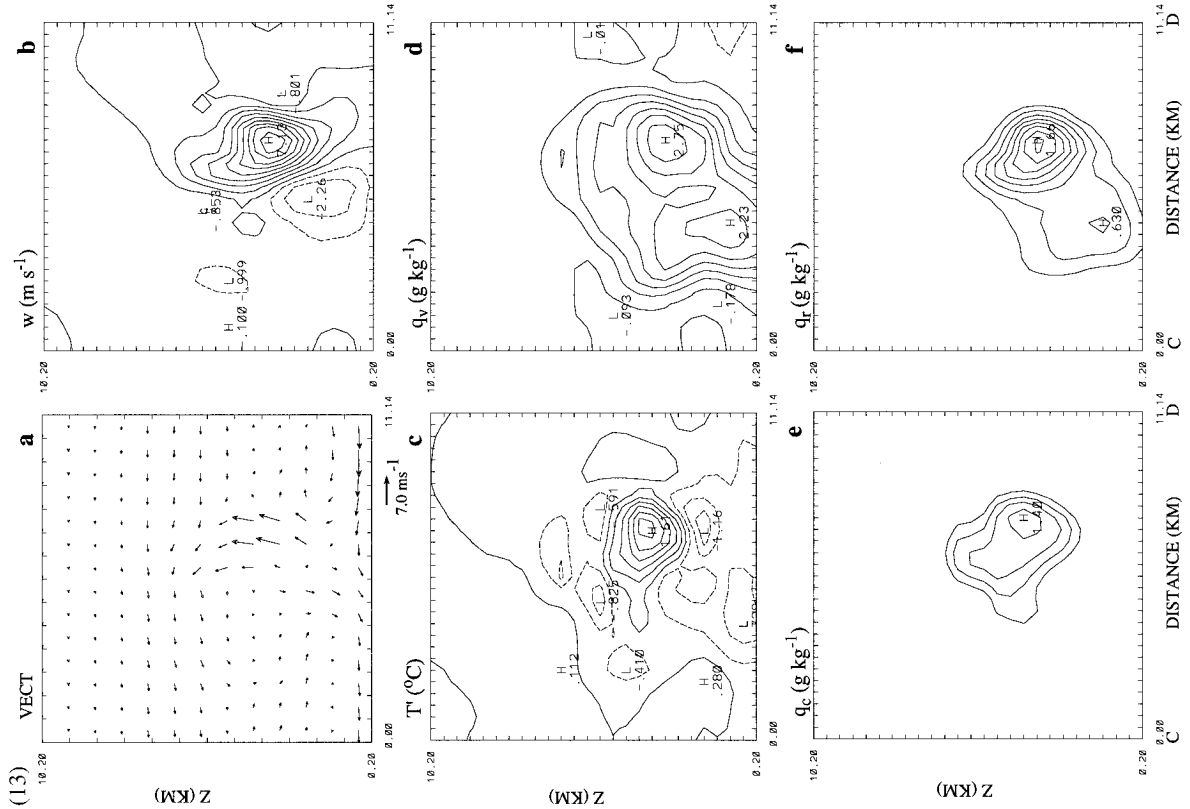

FIG. 13. Same as Fig. 11 but from experiment NTF.

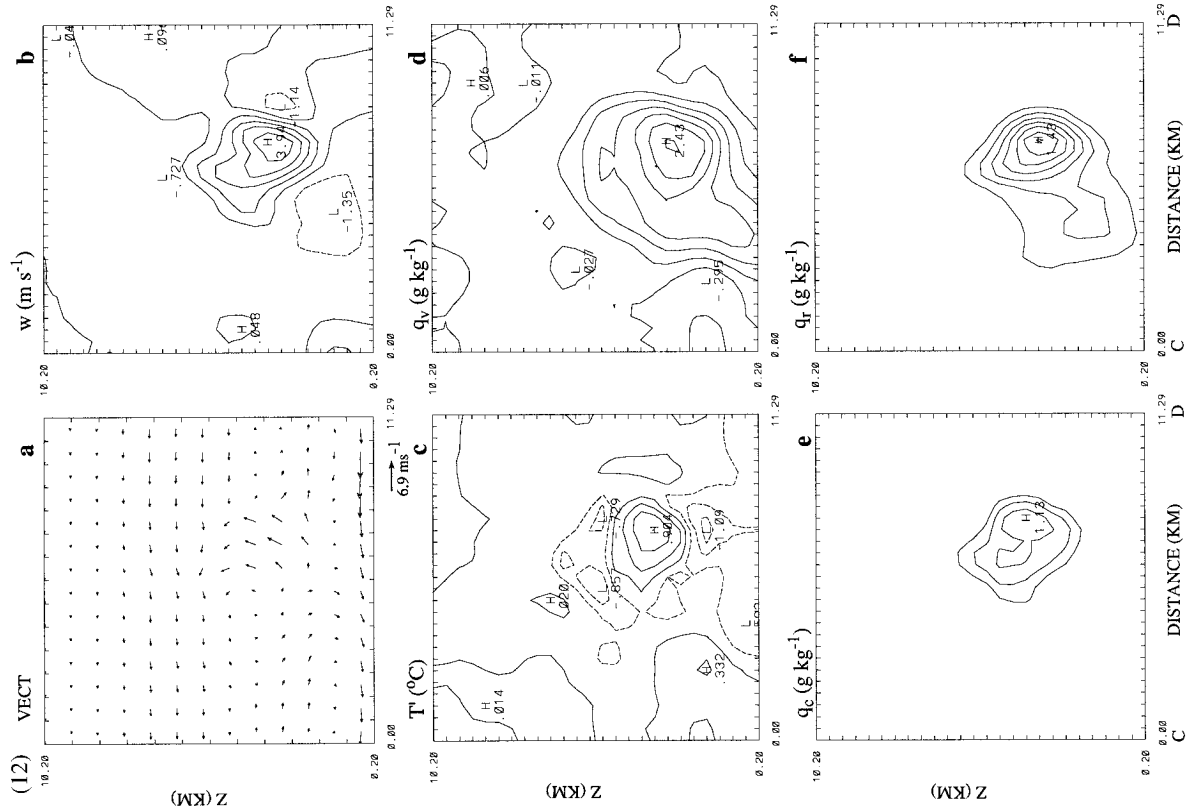

FIG. 12. Same as Fig. 11 but from experiment SGL.

Comparing Fig. 12 with Fig. 11, it is found that the main structure of the storm is retrieved from experiment SGL in which data from CP-3 are excluded. The primary difference between experiment SGL and experiment CTR is the reduced peak strength in almost all of the six fields. Differences in the peak values are on the order of 10% within the rain core. A possible explanation for the reduced strength in experiment SGL is that the decrease of the amount of velocity information results in a weaker divergence field, hence a weaker vertical velocity field, which, in turn, causes less condensation effect. Therefore, less cloud water and rainwater are produced, although the water vapor perturbation is slightly larger than that in experiment CTR.

A closer examination reveals that a larger difference occurs in the downdraft region than in the updraft region. This is largely due to the smaller rainwater content in that region. The cost function measures the misfit between the model prediction and the observations of both the radial velocity and the rainwater mixing ratio. If the rainwater content is small, more weight is put on the velocity observations. Therefore, more sensitivity can result from the suspension of velocity data from one radar. A similar experiment was conducted using CP-3 data only and the retrieved fields were very close to those from experiment SGL in which only CP-4 data were assimilated. These experiments indicate that VDRAS works successfully when information from a single-Doppler radar is provided and the results are relatively independent of viewing angle.

c. No time field

In the above experiments, we have used a time field for each data volume to record the collection time of the data at each grid point and injected the data into the retrieval system at the time step closest to its collection time. A common practice in radar analysis is to assign a fixed time to each radar volume and then to advect the data at each grid point according to the propagation velocity of the storm of interest. For the convective system of our interest, we found this was difficult to do because the two cells in the system did not have a common propagation velocity. Besides, this type of advection method can not take into account the evolution of the field of radial velocity. Furthermore, for a vector field such as radial velocity, a simple advection scheme will cause errors in the advected field. [However, if a radar volume has a short time span (as in our case), the advected field will not be significantly affected due to the remapping of the advected field to the regular analysis grid (J. Miller 1996, personal communication)]. In experiment NTF, we test the sensitivity of the radar analysis to the neglect of the time difference. Rather than using the time field to specify the observation time for each data point, a fixed time was given to the radar volume V2 (1911:49 UTC) and to volume V3 (1916:21 UTC). No data advection was performed. The assimilation length was reduced to 5 min 32 s. In Fig. 13 the retrieved fields are illustrated by the vertical cross sections. Comparing Fig. 13 with Fig. 11, significant differences are shown in the vertical velocity and buoyancy fields. The updraft is more than 2 m s^{-1} stronger than in experiment CTR and the downdraft is weaker. The temperature excess increases by more than 50%. The differences in the microphysical fields are relatively small. These results indicate that the horizontal divergence of the wind is very sensitive to the neglect of the time difference in a radar volume, which, in turn, causes a sensitive response to the vertical velocity and buoyancy fields.

d. Inclusion of the background term

In experiment CTR, the three data volumes V1, V2, and V3 were assimilated successively. That is, the data volumes V1 and V2 were assimilated in period I, and the data volumes V2 and V3 were assimilated in period II. The two assimilation periods are overlapped during the time spanned by the volume V2. Since the model does not match the observations perfectly and the information obtained from the observations is not complete, it is natural to expect some differences between the retrieved fields from the two assimilation runs in the overlapping time. These differences can be reduced by the inclusion of the background term J_{bm} in the cost function. In the final experiment, experiment BKG, we attempt to examine the effect of the background term J_{bm} by using the retrieval output at t = 1910:34 from the assimilation period I as the background at the start of the assimilation period II. By doing so, we expect that the information before the initial time of the current assimilation period can be incorporated and hence the retrieval can be improved. The weighting coefficient η_{0m} in the background term J_{bm} was chosen in the following manner. The coefficients for velocities are set to 1, the same as the dimensional constant S_v in η_v, and the coefficient for rainwater mixing ratio are set to 100, the same as the dimensional constant S_q in η_q; the coefficients for all the other fields (q_t, θ_l, q_c, T'), for which no observations are available, are set to 10. The results from the experiment BKG show that, at the final time of the assimilation period, the differences between the retrievals from the experiment CTR and the experiment BKG are quite small. The effect of this background term is greatest at the initial time of the assimilation period and decreases with integration time. The retrieved fields from experiment CTR and the experiment BKG at t = 1911:49 UTC are shown in Figs. 14 and 15, respectively. Clearly, the retrieved fields from experiment BKG are smoother than those from the experiment CTR. When we compare Figs. 14 and 15 with Fig. 10, the retrieved fields at the same time but from the assimilation period I, it is found that the retrieved fields in Fig. 15 are closer to those in Fig. 10. Although we do not have detailed data to verify whether the inclusion of the background

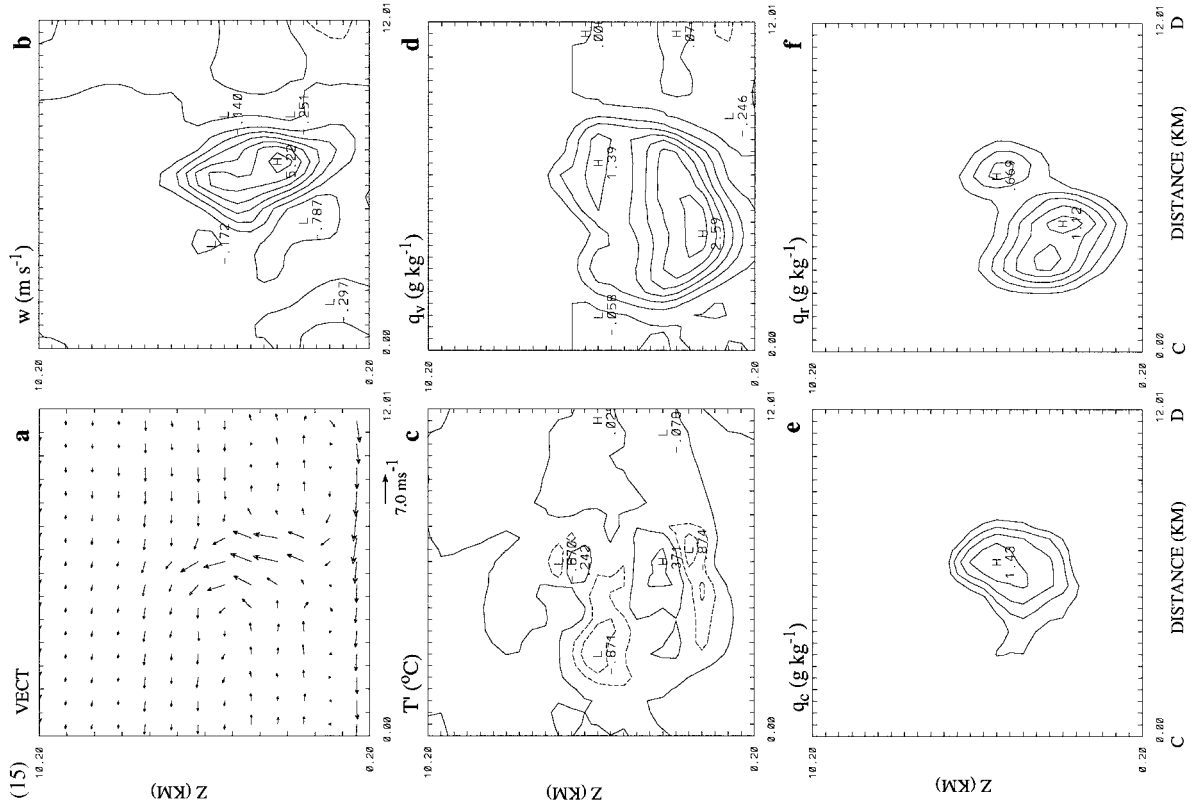

FIG. 15. Same as Fig. 14 but from experiment BKG.

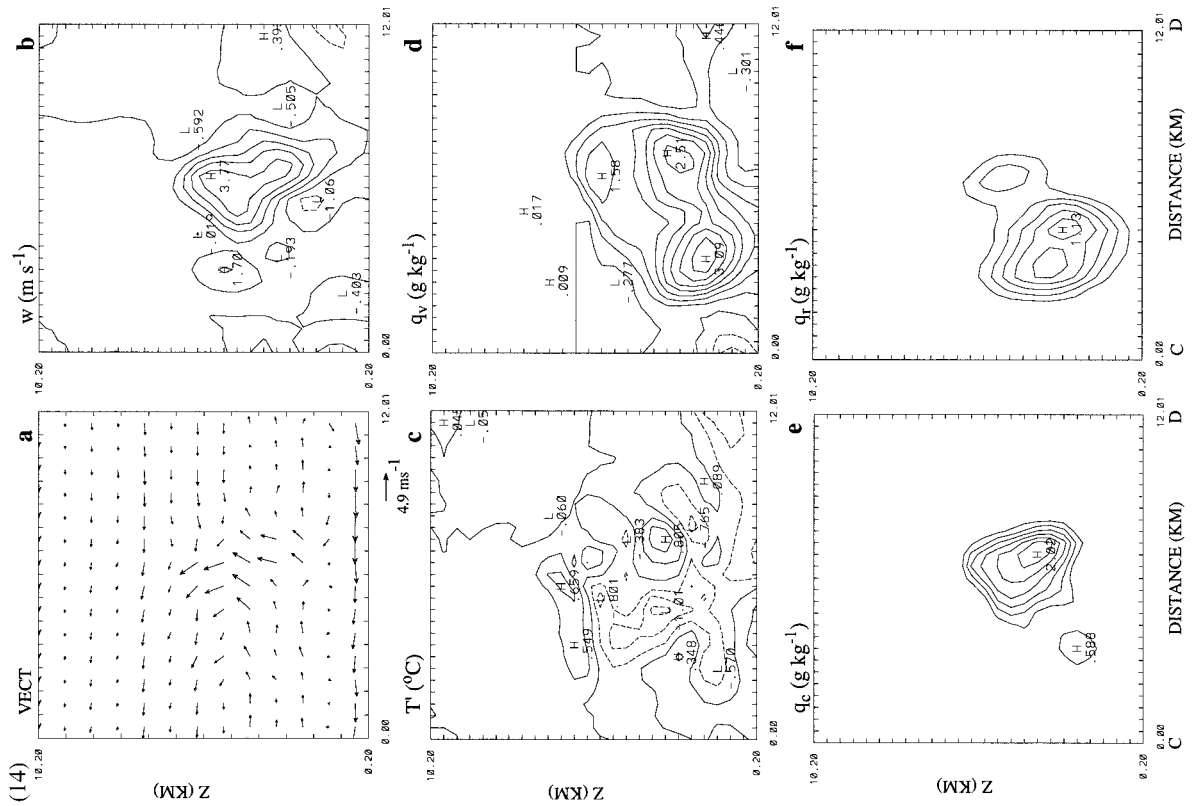

FIG. 14. Same as Fig. 10 but from run 2 of experiment CTR.

term improved the retrieval, it is evident that the discontinuity between the two assimilation runs is reduced and smoother fields are obtained. This may have an important impact on subsequent numerical forecasts when the retrieved fields are used as initial conditions.

It should be noted that since the background field was obtained in the assimilation period I using observations V1 and V2, there is a correlation between the background and the observations in the assimilation period II. The above experiment implied that this correlation was ignored for practical purposes. Further investigations on how to create the most appropriate background field are certainly required.

5. Comparison with aircraft data

During the lifetime of this storm, nearly simultaneous penetrations were made by the two King Airs, Wyoming (N2UW) at a level of 3.0 km and NCAR (N312D) at a level of 4.8 km. Figure 16 shows the two aircraft tracks between 1909:00 UTC and 1918:00 UTC along with the reflectivity observed by CP-4 at 1911:49 UTC at these two heights. The segment used for the comparison is marked by the thick line in the figure. Although the two aircraft are equipped with different types of instruments, they both provide measurements of wind, temperature, humidity, and microphysical parameters, among others. The smallest particles are measured by the forward scattering spectrometer probe (FSSP) cloud droplet probe (size range of 0.5–47 μm). Detection and measurement of the larger particles are done with the 2D cloud (2DC) and precipitation (2DP) probes. These two probes are designed to measure drops greater than 25 and 200 μm, respectively.

The wind measurements are made using a pressure port radome on the NCAR King Air and a gust probe on the Wyoming King Air. Both systems provide quite accurate wind measurements. However, greater uncertainty may exist in the temperature, humidity, and microphysical measurements. The FSSP is believed to underestimate the liquid water content due to problems such as having more than one particle coincident in the beam, particles passing through the beam while the sensor is processing the data from the previous particle, inadequate response time of the pulse height analyzers, and laser beam inhomogeneities. The incloud temperature and humidity measurements may suffer from evaporative cooling at these sensors. Consequently, the incloud temperature can be underestimated and the humidity can be overestimated. For a detailed discussion on the quality of the King Air data, the reader is referred to Barnes et al. (1996).

Before we proceed to make the comparison, it is important to note that a one to one correspondence should not be expected in comparing data from the two different systems. Besides the uncertainties in the aircraft measurements and fluctuations caused by possible small excursions the aircraft may experience, the different resolution between the King Air data and the retrieval system is another problem that can set a limit to the comparison. The smallest resolvable scale in a numerical model is $4\Delta x$ (or 1600 m in our study). On the other hand, sampling at 1 Hz combined with an airspeed of slightly less than 100 m s^{-1} yields a horizontal resolution of nearly 100 m for the aircraft data. In order to obtain a similar resolution for the data from the two systems, a running smoother is applied to the aircraft data to produce smoothed aircraft data with a similar resolution to the model data. In the following, we will compare

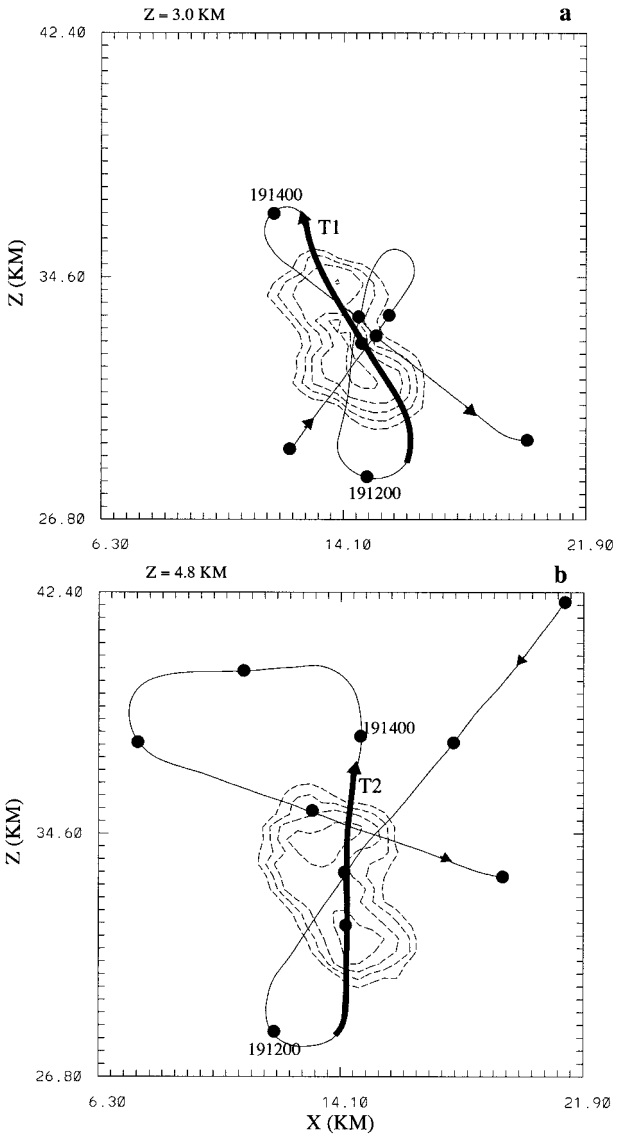

FIG. 16. Aircraft tracks of (a) the Wyoming King Air N2UW at 3.0 km from 1909 UTC to 1916 UTC and (b) NCAR King Air N312D at 4.8 km from 1909 UTC to 1918 UTC. The heavy lines with arrows mark the segments of the tracks used for comparison with the retrieved fields. The dots show 1-min positions along the tracks. Reflectivity contours with an interval of 10 dB at 1911:49 UTC are superimposed.

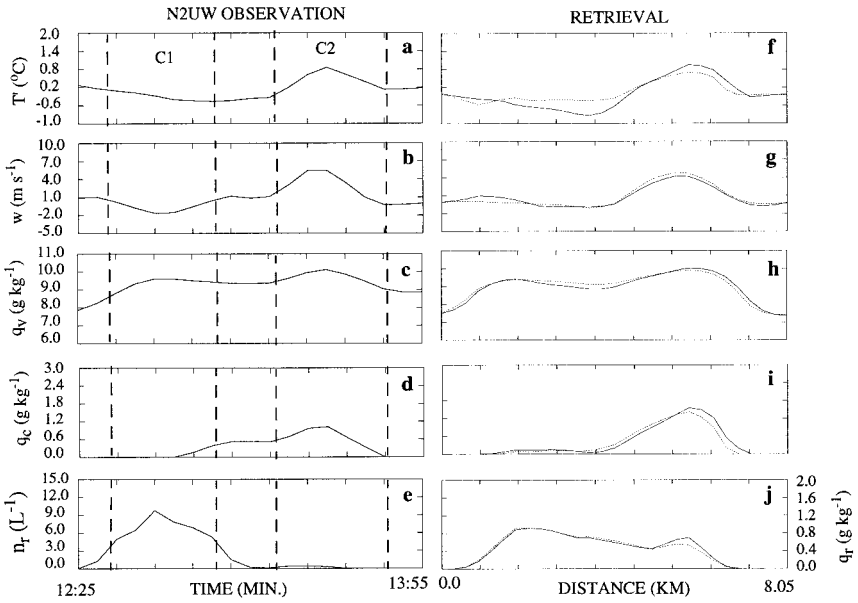

FIG. 17. The left panels show time series of the aircraft observed fields along the N2UW track (at $z = 3.0$ km) between 1912:25 UTC and 1913:55 UTC. The displayed fields are (a) perturbation temperature; (b) vertical velocity; (c) water vapor mixing ratio; (d) mixing ratio of cloud droplets; and (e) number concentration of large drops. The right panels show the retrieved fields along the same track at 1913:10 UTC from experiment CTR (solid line) and experiment BKG (dotted line). The same fields are displayed as in the left panels, except in the last panel where the retrieved rainwater mixing ratio is shown.

the retrieval with the smoothed data. We will focus our attention to experiments CTR and BKG in the comparison.

The N2UW and N312D King Air data are shown in the left panels in Figs. 17 and 18, respectively. The N2UW data are between 1912:25 UTC and 1913:55 UTC and the N312D data are between 1912:30 UTC and 1914:00 UTC. The tracks of the two aircraft at these

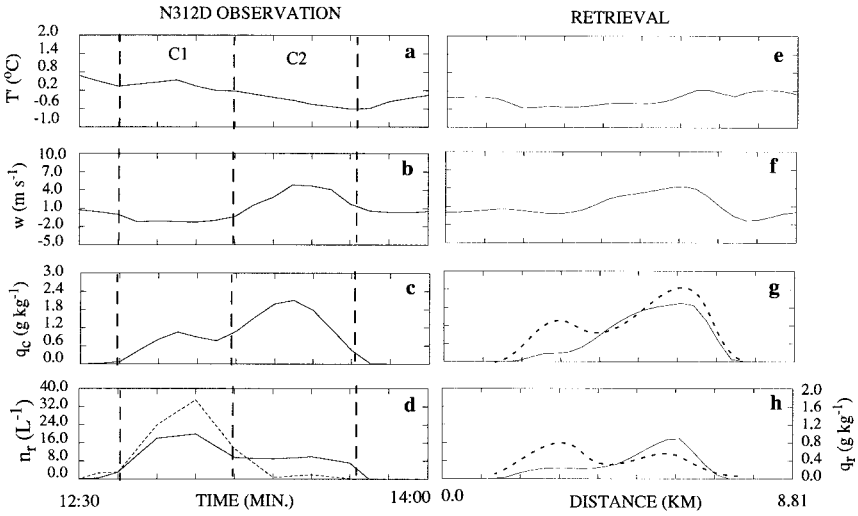

FIG. 18. The left panels show time series of the aircraft observed fields along the N312D track (at $z = 4.8$ km) between 1912:30 UTC and 1914:00 UTC. The displayed fields are (a) perturbation temperature; (b) vertical velocity; (c) mixing ratio of cloud droplets; and (d) mixing ratio (solid line) and number concentration (dashed line) of large drops. The right panels show the retrieved fields along the same track at 1913:10 UTC. The same fields are displayed as in the left panels, except in the last panel where the retrieved rainwater mixing ratio is shown. The dashed line in (g) and (h) represents the result from the experiment using a q_r/Z–Z_{DR} relation.

periods are illustrated in Fig. 16 by the heavy lines and labeled by T1 and T2. Along these tracks, the King Airs penetrated both cells approximately through their centers. Note that the superimposed reflectivity contours in Fig. 16 are from V2, which covers a period earlier than the aircraft tracks T1 and T2 do (see Fig. 7 for the configuration). In Figs. 17a–e, the perturbation temperature, the vertical velocity, the water vapor mixing ratio, the cloud water mixing ratio, and the number concentration of larger drops from N2UW are displayed. The cloud water mixing ratio is derived from the FSSP data and the concentration of larger drops is the combination of 2DC and 2DP measurements. Since the water vapor mixing ratio data from N312D showed obvious errors, this quantity is not displayed in Fig. 18. In Fig. 18d, the mixing ratio (solid line) of the larger drops is shown in addition to the number concentration (dashed line). Due to an error in attempting to obtain the median mass diameter from the tape for N2UW data, we were not able to convert the number concentration observed by N2UW into a mixing ratio. The dashed vertical lines in these two figures denote cell boundaries based on the original unsmoothed data.

At the 3-km level (Figs. 17a–e), the N2UW data clearly show a temperature excess of 0.8°C and an updraft of about 5 m s^{-1} within cell C2, and a weak downdraft within cell C1. The cloud mixing ratio in C2 peaks at the value of around 1 g kg^{-1} while only a small amount of cloud water remains in C1. In contrast, significant concentrations of larger drops are evident from the 2DC and 2DP probes in C1 while there are almost no raindrops in C2. Unlike the other fields, there is not a clear distinction in water vapor mixing ratio between the two cells. Instead, a broad zone of excess q_v is more evident. At the 4.8-km level (Figs. 18a–d), the updraft in C2 is accompanied by a high cloud water mixing ratio of over 1.8 g kg^{-1} but not by a temperature excess as at the 3-km level. Similar to the observations at the 3-km level, there is a very small amount of precipitation in C2. However, the cloud water is somewhat larger than at 3 km in both cells, indicating less cloud droplet depletion at the higher altitude.

To compare the retrieval with the N2UW and N312D data, the variation of the corresponding fields along the tracks T1 at $z = 3$ km and T2 at $z = 4.8$ km at 1913: 10 UTC are shown in the right panels of Figs. 17 and 18. It should be noted that since the retrieved fields are available at every time step during the assimilation period, we could use the time sequence rather than using retrieved values at a fixed time for comparison. However, we have found that the differences between the time sequence plot and the fixed time plot are very small. For convenience, we have chosen to use the fixed time plot for comparison. The solid lines in the two figures are plotted using data from experiment CTR and the dotted lines in Fig. 17 from experiment BKG. The dashed lines in Figs. 18g and 18h show the retrieval using the rainwater mixing ratio obtained from Z_{DR} measurements, which will be explained later in this section. Similar to the N2UW data, the updraft in cell C2 is accompanied by a temperature excess and a large concentration of cloud water. The strength of the updraft from both experiments is weaker than that shown by the N2UW data. The difference in the maximum value of the vertical velocity is about 1 m s^{-1} for experiment BKG. The temperature excess in cell C2 from experiment CTR is around 1°C, slightly higher than that shown in Fig. 17a. However, this value is reduced in experiment BKG and results in a value closer to the N2UW measurement (~0.8°C). The temperature minimum of ~−0.8°C in experiment CTR is also corrected in experiment BKG. The retrieved cloud water mixing ratio from experiment BKG shows a maximum of ~1.4 g kg^{-1}, which is about 0.4 g kg^{-1} higher than the N2UW measurements. Both the retrieval and the N2UW observations demonstrate that cell C1 consists mostly of large raindrops and the cloud water is almost completely depleted. The water vapor mixing ratio shows good agreement with observations except for the portion outside the cell C2. The greatest difference between the retrieval and the N2UW data is shown in the rainwater in cell C2. A significant amount of rainwater in C2 is obtained from the retrieval, while there is hardly any concentration of raindrops in C2 from the N2UW measurement. At the 4.8-km level (Fig. 18), an updraft of ~4.0 m s^{-1} is evident from both the retrieval and the observations. Although the perturbation temperature does not agree very well on a one to one basis, neither the retrieval nor the observations shows a cell structure. The amount of cloud water (solid line) in C2 is very close to the observations, while it is much smaller than the observation in C1. Contrary to the aircraft measurement, the retrieved rainwater mixing ratio (solid line) indicates that cell C2 contains more rainwater than cell C1.

The disagreement in the rainwater field between the retrieval and the observation is somewhat surprising when we consider the fact that the rainwater mixing ratio is an input quantity in the cost function. If the Z–q_r relation gives a reasonable estimation of the rainwater mixing ratio and the minimization process is able to produce a good fit between the model solution and the corresponding input field, the retrieved rainwater mixing ratio should be a good representation of the reflectivity observations. In Fig. 19, the evolution of the retrieved rainwater mixing ratio through the center of the two cells is presented. The dashed contours in Figs. 19a and 19c illustrate the observations of the rainwater mixing ratio that are derived from V2 and V3 of the reflectivity observations, respectively. The retrieved field resembles the radar-derived field, indicating the model solution of the rainwater mixing ratio is fitted to the observations rather closely. The retrieved rainwater mixing ratio is smoother and hence the maximum values are smaller than the radar-derived field. From Fig. 19, it is evident that the precipitation starts at high altitude and increases

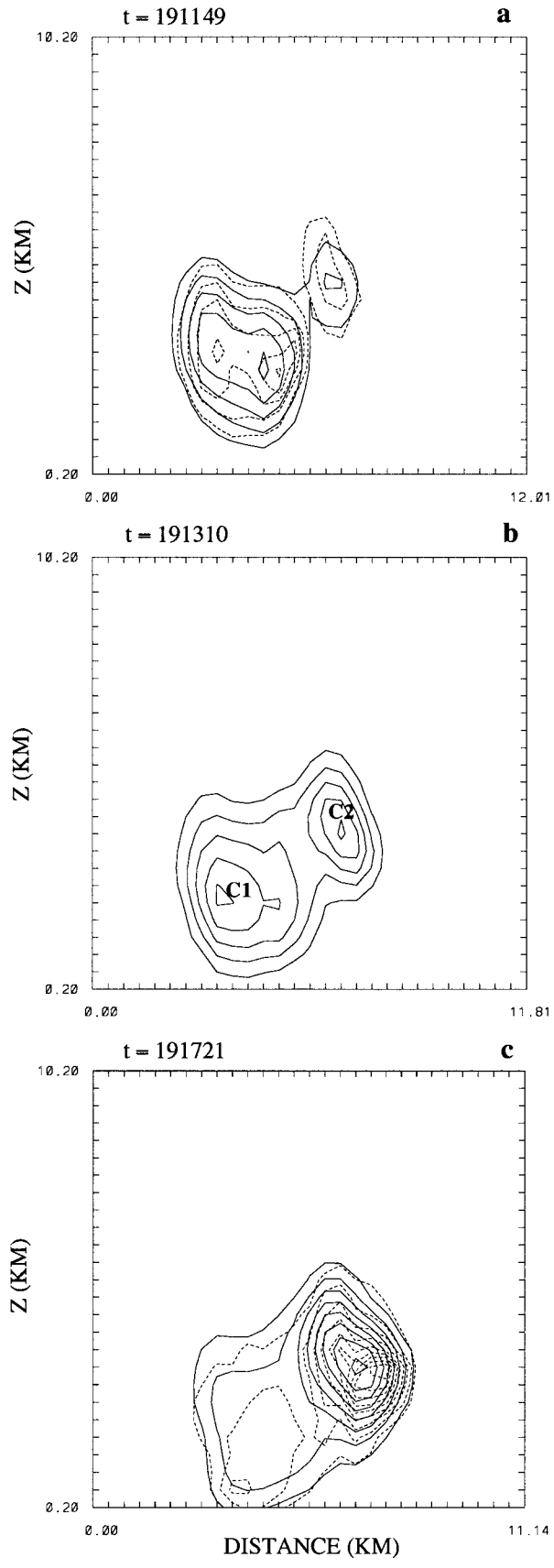

rapidly as it descends. At 1911:49, before the King Airs fly through the storm, there exists a small amount of rainwater centered at $z = 5.0$ km (the reflectivity is over 30 dBZ). At 1913:10, the midtime of the King Airs' flight through the storm, the retrieved field shows that about 1 g kg^{-1} of rainwater is accumulated in cell C2 while both precipitation cores descend to lower levels. It is obvious that the amount of rainwater in C2 at higher levels exceeds that in C1.

The above examination leads us to attribute the disagreement of the rainwater mixing ratio to the inaccuracy of the input data, or in other words, the inadequate estimate of the observational error covariance. The rainwater mixing ratio derived from the Z–q_r relation may contain errors arising from two possible sources: the reflectivity calibration error and the use of approximate Z–q_r relationships. Although the reflectivity calibration error can be significant, it is difficult to evaluate it. To determine whether the Z–q_r relation gave a good estimate of the rainwater mixing ratio, we examined the differential reflectivity (Z_{DR}) data from CP-2. Studies have shown that the rainfall rate and the rainwater content determined using Z_{DR} is more accurate than using the reflectivity, since Z_{DR} contains drop-size information (e. g., Seliga et al. 1986; Tuttle et al. 1989). Figure 20 shows the Z_{DR} field (solid line) through the N312D flight track at approximately the same time as the aircraft flight time. The reflectivity field from CP-2 is overlaid. Since the value of Z_{DR} approximately represents the size of the raindrops in mm (Bringi et al. 1986; Wakimoto and Bringi 1988), Fig. 20 suggests that cell C2 contains mostly large drops while the cell C1 consists of smaller drops, although similar reflectivity magnitude is observed in both cells. Careful examination of the aircraft data confirmed this finding and indicated that the two cells have different drop-size distributions. Since the Z–q_r relation assumes a Marshal–Palmer drop size distribution defined by two parameters, it is unable to accurately determine the rainwater mixing ratio in both cells. Using the following empirical relationships between Z_{DR} and q_r/Z for a heavy rainfall event in central Illinois,

$$\frac{q_r}{Z} = 7.38 \times 10^{-5} Z_{DR}^{-1.92}, \qquad (5.1)$$

obtained by Seliga et al. (1986), we recomputed the rainwater mixing ratio. The result indicated that, with the same magnitude of the reflectivity, the calculation yielded less rainwater in cell C2 than in cell C1 due to the larger drop size in C2, which is consistent with the aircraft measurements. However, the magnitude of the

←

FIG. 19. Vertical cross section of retrieved rainwater mixing ratio and derived rainwater mixing ratio [dotted contours in (a) and (c)] using Z–q_r relation through the center of the storm at (a) 1911:49 UTC, (b) 1913:10 UTC, and (c) 1917:21 UTC.

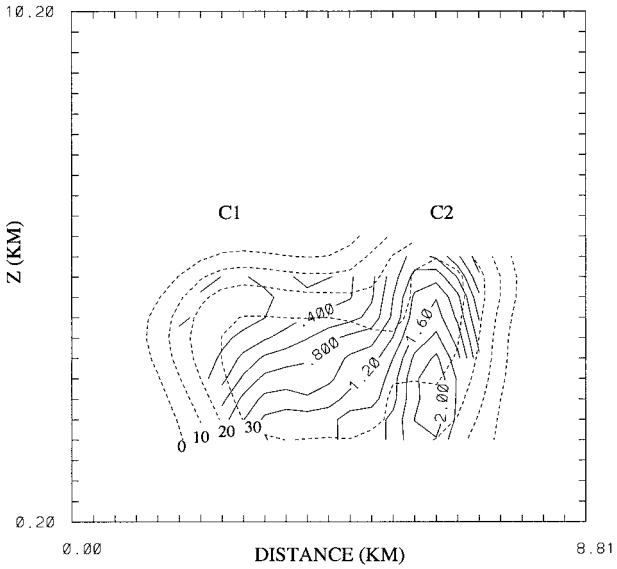

FIG. 20. Vertical cross section of the observed reflectivity (dashed line) and differential reflectivity (solid line) from CP-2 along the N312D track.

calculated rainwater using Eq. (5.1) is smaller than the aircraft measurement in both cells by about 30%. Using the radar-observed Z and Z_{DR} and the rainwater mixing ratio derived from the aircraft observations, we performed a least square fit to determine the appropriate constants in relation Eq. (5.1). The result is given by

$$\frac{q_r}{Z} = 2.3 \times 10^{-4} Z_{DR}^{-1.16}. \quad (5.2)$$

If the error in the derived rainwater mixing ratio plays a major role in the disagreement of the microphysical fields between the aircraft measurements and the retrieval, the rainwater mixing ratio derived using Eq. (5.2) should then bring the retrieved microphysics much closer to the aircraft measurements. Applying relation Eq. (5.2), we calculated the rainwater mixing ratio and used it to conduct a retrieval experiment. In this experiment, we indeed found substantial change in the microphysical retrieval. As shown by the dashed line in Figs. 18g and 18h, not only is the rainwater field in closer agreement to the aircraft measurements but also the retrieved cloud water field. This experiment indicates that the microphysical retrieval is quite sensitive to the derived input field of rainwater mixing ratio and it is important to obtain an accurate estimation of the rainwater mixing ratio.

6. Summary and discussions

In this paper, the ability of VDRAS in dynamical and microphysical retrieval was examined using data from a Florida airmass storm that occurred during CaPE. This storm consisted of two convective cells. The assimilation was performed during the developing stage of cell C2. A control experiment was conducted using data collected by CP-3 and CP-4. Three radar volumes were assimilated into the analysis system in two separate assimilation runs. The radar data at each grid point were injected into the system according to the collection time. In addition to the control experiment, three experiments were conducted using data from only one radar, injecting each radar volume at a fixed time, and including a background term provided by the previous assimilation run. The retrieved fields were compared with measurements obtained by the NCAR and Wyoming King Airs. The experimental results suggested that a dynamically consistent structure of the convection can be obtained using information from one or two radars. However, the strength of the retrieved fields using information from only one radar is weaker. The differences of the peak values in the rain core are on the order of 10%. The comparison with the aircraft measurements demonstrated that the general structure and strength of the convective system was retrieved quite well, but less agreement between the retrieved microphysical fields and their aircraft measurements was found. The poor estimation of the rainwater mixing ratio from the reflectivity observations was found to be the primary cause for the disagreement in the microphysical fields.

The experiment NTF indicated that the retrieval can be quite sensitive to the neglect of the time difference between grid points in a radar volume. The difference between this experiment and experiment CTR was as large as 50% for the vertical velocity and perturbation temperature fields. This finding has an important application to airborne Doppler radars. It is typical for an airborne Doppler radar volume to have a longer time span than most ground-based radars. The ability of the VDRAS in assimilating the radar observations at their actual collection time makes this technique appealing to the analysis of airborne Doppler radar data.

In both parts of this study, we have addressed the importance of the background information. In part I, we examined the background term J_{bs}, which constrains the model solution in data-void regions toward the mean state given by an upper-air sounding. In this paper, we tested the effect of the background term J_{bm}, which constrains the model solution toward the background information provided by a previous model run valid at the initial time of the assimilation period. Both tests demonstrated the importance of incorporating background information in VDRAS. These studies on the implementation of the background terms were very preliminary, however, since error covariance matrices were assumed diagonal. More sophisticated schemes for the background term are needed in order to properly specify the mesoscale balance in the storm environment.

Although we are reasonably encouraged by the results obtained in this study, great challenges are still present in further application of this technique. Although the case we studied in this paper has most of the characteristics of a typical convective storm, it is certainly not

representative of all convective storms, especially deep convection. Therefore, it is important to point out that our conclusions are only pertinent to this particular case. Since microphysical processes play an important role in numerical modeling of convective storms, errors in parameterization of these processes can cause difficulties in fitting the model to data and thus result in significant retrieval errors. This problem can be more prominent when more intense storms are studied. The use of approximate Z–q_r relationships is another limitation to the accuracy of the retrieval. Like the parameterization error, the error in the derived rainwater mixing ratio can be more troublesome for severe storms. In this study, we have demonstrated that the use of q_r/Z–Z_{DR} relation improved the estimate of the rainwater mixing ratio and hence the microphysical retrieval. This result suggests the need for dual polarization observations of Doppler radars.

Future work will be carried out on the retrieval of the unobserved fields in more intense storms. A supercell storm from Verification of the Origins of Rotation in Tornadoes Experiment will be studied to examine the applicability of the technique to severe thunderstorms. The current warm rain model will be extended to consider the ice effect involved in a deeper storm. More sophisticated and appropriate background specifications with error statistics need to be incorporated into the system. With stronger instabilities and more sensitivities to the microphysical parameterization schemes and to the approximation of the rainwater conversion relation, the retrieval of the unobserved fields in more intense storms present greater challenges.

Acknowledgments. This research is sponsored by the National Science Foundation through an Interagency Agreement in response to requirements and funding by the Federal Aviation Administration's Aviation Weather Development Program. The views expressed are those of the authors and do not necessarily represent the official policy or position of the U.S. government. The authors are grateful to J. Fankhauser, D. Breed, and R. Ames for their help with the aircraft data, and to J. Tuttle for his help in interpreting the differential reflectivity data. Thanks are also due to John Tuttle and Francois Vandenberghe for review of this paper.

REFERENCES

Barnes, G. B., and W. Browning, 1993: Is there significant lateral mixing in convective clouds? *Proc. 20th Conf. on Hurricanes and Tropical Meteorology*, San Antonio, TX, Amer. Meteor. Soc. 70–73.

——, ——, and J. C. Fankhauser, 1992: The evolution of cumulus congestus in a low shear, high instability environment: CaPE aircraft analyses. *Proc. 11th Conf. on Clouds and Precipitation*, Montreal, Quebec, Canada, Amer. Meteor. Soc., 440–443.

——, J. C. Fankhauser, and W. D. Browning, 1996: Evolution of vertical mass flux and diagnosed net lateral mixing in isolated convective clouds. *Mon. Wea. Rev.*, **124,** 2764–2784.

Bringi, V. N., R. M. Rasmussen, and J. Vivekanandan, 1986: Multiparameter radar measurements in Colorado convective storms. Part I: Graupel melting studies. *J. Atmos. Sci.*, **43,** 2545–2563.

Fankhauser, J. C., and D. W. Breed, 1995: Vertical mass flux and precipitation development observed during the life cycle of a Florida cumulus congestus. *Proc. 27th Conf. on Radar Meteorology*, Vail, CO, Amer. Meteor. Soc., 380–382.

Gal-Chen, T., 1978: A method for the initialization of the anelastic equations: Implications for matching models with observations. *Mon. Wea. Rev.*, **106,** 587–606.

Hane, C. E., and B. C. Scott, 1978: Temperature and pressure perturbations within convective clouds derived from detailed air motion information: Preliminary testing. *Mon. Wea. Rev.*, **106,** 654–661.

——, R. B. Wilhelmson, and T. Gal-Chen, 1981: Retrieval of thermodynamic variables within deep convective clouds: Experiments in three dimensions. *Mon. Wea. Rev.*, **109,** 564–576.

Hauser, D., and P. Amayenc, 1986: Retrieval of cloud water and water vapor contents from Doppler radar data in a tropical squall line. *J. Atmos. Sci.*, **43,** 823–838.

Laird, N. F., D. A. R. Kristovich, R. M. Rauber, H. T. Ochs III, and L. J. Miller, 1995: The Cape Canaveral sea and river breezes: Kinematic structure and convective initiation. *Mon. Wea. Rev.*, **123,** 2942–2956.

Leise, J. A., 1981: A multidimensional scale-telescoped filter and data extension package. NOAA Tech. Memo. ERL/WPL-82, 20 pp. [Available from Wave Propagation Laboratory, 325 Broadway, Boulder, CO 80303.]

Miller, L. J., C. G. Mohr, and A. J. Weinheimer, 1986: The simple rectification to Cartesian space of folded radial velocities from Doppler radar sampling. *J. Atmos. Oceanic Technol.*, **3,** 162–174.

Mohr, C. G., and R. L. Vaughan, 1979: An ecomomical procedure for Cartesian interpolation and display of reflectivity data in three dimensional space. *J. Appl. Meteor.*, **18,** 661–670.

——, L. J. Miller, R. L. Vaughan, and H. W. Frank, 1986: The merger of mesoscale datasets into a common Cartesian format for efficient and systematic analyses. *J. Atmos. Oceanic Technol.*, **3,** 144–161.

Roux, F., 1985: Retrieval of thermodynamic fields from multiple-Doppler radar data using the equations of motion and the thermodynamic equation. *Mon. Wea. Rev.*, **113,** 2142–2157.

Rutledge, S. A., and P. V. Hobbs, 1983: The mesoscale and microscale structure and organization of clouds and precipitation in midlatitude cyclone. VIII: A model for the ''seeder-feeder'' process in warm-frontal rainbands. *J. Atmos. Sci.*, **40,** 1185–1206.

——, and ——, 1984: The mesoscale and microscale structure and organization of clouds and precipitation in mid-latitude cyclone. XII: A diagnostic modeling study of precipitation development in narrow cold-frontal rainbands. *J. Atmos. Sci.*, **41,** 2949–2972.

Seliga, T. A., K. Aydin, and H. Direskeneli, 1986: Disdrometer measurements during an intense rainfall event in central Illinois: Implications for differential reflectivity radar observations. *J. Appl. Meteor.*, **25,** 835–846.

Sun, J., and N. A. Crook, 1994: Wind and thermodynamic retrieval from single-Doppler measurements of a gust front observed during Phoenix II. *Mon. Wea. Rev.*, **122,** 1075–1091.

——, and ——, 1997: Dynamical and microphysical retrieval from Doppler radar observations using a cloud model and its adjoint. Part I: Model development and simulated data experiments. *J. Atmos. Sci.*, **54,** 1642–1661.

Tuttle, J. D., V. N. Bringi, H. D. Orville, and F. J. Kopp, 1989: Multiparameter radar study of a microburst: Comparison with model results. *J. Atmos. Sci.*, **46,** 601–620.

Wakimoto, R. M., and V. N. Bringi, 1988: Dual-polarization observations of microbursts associated with intense convection: The 20 July storm during the MIST project. *Mon. Wea. Rev.*, **116,** 1521–1539.

Ziegler, C. L., 1985: Retrieval of thermal and microphysical variables in observed convective storms. Part I: Model development and preliminary testing. *J. Atmos. Sci.*, **42,** 1487–1509.